
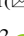






Integrity Monitoring of PPP-RTK Based on Multiple Hypothesis Solution Separation

Shizhuang Wang¹ , Xingqun Zhan¹  , Yingchao Xiao¹,
and Yawei Zhai² 

¹ Shanghai Jiao Tong University, Shanghai 200240, China
xqzhan@sjtu.edu.cn

² GeeSpace Co. Ltd., Shanghai 200240, China

Abstract. Recent progress for high-precision positioning mainly focused on PPP-RTK, which is a precise point positioning (PPP) technique based on a real-time kinematic (RTK) network. PPP-RTK is expected to become the mainstream positioning solution for various intelligent transportation systems (ITS) such as autonomous driving, unmanned aerial vehicles, and urban air mobility. Prior studies on PPP-RTK mainly focused on improving navigation accuracy. However, for safety-critical applications, integrity is also an important performance index. Since PPP-RTK is usually implemented using a Kalman filter (KF), the well-known integrity monitoring schemes developed for least-squares-based systems cannot be directly applied to PPP-RTK. After considering the time-sequential nature of KF, we propose a user-end integrity monitoring scheme of PPP-RTK based on multiple hypothesis solution separation (MHSS) to offer high-reliability and high-precision position solutions with real-time integrity information. The proposed scheme includes two key functions: real-time fault detection and rigorous protection level (PL) evaluation. This scheme captures both the faults from PPP-RTK service products and those faults introduced at the user end. Experiments are carried out with real data and simulated fault scenarios. The results suggest the effectiveness of the proposed scheme and indicate that multi-constellation PPP-RTK can offer position solutions with decimeter-level PLs (integrity risk: $10^{-7}/h$) in open-sky areas.

Keywords: PPP-RTK · Integrity monitoring · Fault detection · Protection level

1 Introduction

Recently, the autonomous systems such as autonomous driving, unmanned aerial vehicles, and urban air mobility, have attracted increasing interest from the industry. Determining the positions is a precondition for these systems to achieve autonomous operations. A wrong positioning solution may lead to extremely dangerous accidents, such as collisions and crashes.

This work was supported by the National Natural Science Foundation of China (62173227, 62103274).

The reliability of navigation systems is usually described by integrity. Integrity measures the confidence level of navigation solutions and reflects the ability to warn users in time when navigation systems are unavailable [1]. The concept of integrity has been put into practice in civil aviation for decades. A variety of user-end integrity monitoring algorithms have been developed, such as Receiver Autonomous Integrity Monitoring (RAIM) [2] and Advanced RAIM (ARAIM) algorithm [3]. In RAIM and ARAIM, Protection Level (PL) is an important performance index, which describes the upper bound of positioning error under acceptable integrity risk. For safety-critical applications, due attention should be paid to integrity aside from accuracy.

To realize Functional Safety (FuSa) of navigation systems, the concept of integrity has recently been extended to other fields, such as autonomous driving. Compared to civil aviation, the navigation performance requirements for novel autonomous applications are generally higher. For example, the Horizontal PL (HPL) should not exceed 1 m for lane-level navigation purpose. Obviously, it is difficult to meet the navigation requirements by using Single Point Positioning (SPP). Thus, high-precision positioning technologies should be considered.

Commonly-used high-precision positioning technologies of Global Navigation Satellite System (GNSS) include Real-Time Kinematic (RTK) [4] and Precise Point Positioning (PPP) [5]. For RTK, the base sends observation data to the rover, and the rover estimates its relative position to the base after eliminating the receiver-independent errors by double difference. PPP does not rely on base stations but uses the precise products such as precise orbits, precise clocks, satellite differential code bias, etc. Recently, PPP-RTK has been developed on the basis of PPP to greatly shorten the convergence time of PPP [6]. Its advantages come from the fact that PPP-RTK further employs the Uncalibrated Phase Delay (UPD) and regional atmosphere products.

PPP-RTK is expected to become the mainstream navigation solution in intelligent transportation applications for the following reasons. First, PPP-RTK greatly reduces the convergence time of PPP from tens of minutes to several epochs. Besides, as compared to RTK, PPP-RTK needs fewer stations to provide the correction services, and thus the service cost is lower. And the user needs not to upload their own positions when they subscribe PPP-RTK services, which is more privacy-friendly. Finally, the reliability of PPP-RTK maybe higher than RTK because it is easier for PPP-RTK to conduct quality control for the service products.

To provide high-precision and high-reliability PPP-RTK navigation solutions, the following three techniques should be considered: server-end integrity monitoring, integrity evaluation of PPP-RTK service products, and user-end integrity monitoring. This paper mainly focuses on the last one. PPP-RTK users may encounter the faults of service products and the receiver-segment faults caused by multipath effects, Non-Line-Of-Sight (NLOS), and undetected cycle slips. The proposed integrity monitoring scheme can protect the navigation system against these faults through real-time fault detection and protection level evaluation.

PPP-RTK usually uses Kalman Filter (KF) as the state estimator, which is different from the Least-Squares (LS) estimator used in SPP. Specifically, LS is snapshot while KF is time-sequential, i.e., KF estimates the current states use both the current and past observations. Although MHSS is developed based on LS, it is applicable to KF-based navigation systems because of the equivalence between a batch LS and KF. Prior

studies have proved the superiority of MHSS over residual-/innovation-based methods for the integrity monitoring of KF-based navigation systems.

Recently, some studies have focused on realizing integrity monitoring for the KF-based navigation systems. For example, Tanil et al. and Wang et al. proposed the MHSS-based integrity monitoring algorithms for GNSS/INS integrated navigation systems [7, 8]; Gunning et al. applied the MHSS method to the integrity monitoring algorithm of PPP [9]. However, to the best knowledge of the authors, there is no user-end integrity monitoring algorithm for PPP-RTK user end in the existing literature. Although the Trimble Company presented their test results about the PLs for the Trimble RTX service-enabled high positioning systems, it is still not clear how the PLs are calculated [10]. Therefore, this paper hopes to make up for the gap in the design of integrity monitoring algorithm for PPP-RTK user end.

2 Fundamentals of PPP-RTK User End

PPP-RTK uses pseudoranges and carrier phases, and they are modeled as:

$$\begin{aligned} \rho_{r,j}^{s,T} = & \|\mathbf{X}^{s,T} - \mathbf{X}_r\| + c(dt_r + isb_r^T - dt^{s,T}) \\ & + Mw_r^{s,T} \cdot ZWD_r + \gamma_j^T \cdot I_{r,1}^{s,T} + (d_{r,j} - d_j^{s,T}) + \varepsilon_{r,j}^{s,T} \end{aligned} \quad (1)$$

$$\begin{aligned} l_{r,j}^{s,T} \triangleq & \lambda_j^{s,T} \Phi_{r,j}^{s,T} = \|\mathbf{X}^{s,T} - \mathbf{X}_r\| + c(dt_r + isb_r^T - dt^{s,T}) \\ & + Mw_r^{s,T} \cdot ZWD_r - \gamma_j^T \cdot I_{r,1}^{s,T} + \lambda_j^{s,T} \cdot (N_{r,j}^{s,T} + b_{r,j} - b_j^{s,T}) + \xi_{r,j}^{s,T} \end{aligned} \quad (2)$$

where s, r, j , and T denote the satellite, receiver, signal, constellation, respectively; ρ is the pseudorange, Φ is the carrier phase; \mathbf{X} is the satellite/receiver position; c is the speed of light; dt is the satellite/receiver clock offset; isb is the inter-system bias; ZWD is the zenith wet troposphere delay, and Mw maps ZWD to the line of sight; I is the slant ionosphere delay, and γ is a frequency-dependent factor; d is Uncalibrated Code Delay (UCD); λ is the carrier wavelength; N is integer ambiguity; b is the UPD; ε and ξ are pseudorange and carrier noises, respectively, including noises that can be modeled (e.g., dry troposphere delay, phase windup, etc.) and those that cannot be modeled. Table 1 summarizes the commonly-used navigation state dynamics models.

Standard PPP requires real-time precise orbit, precise clock and DCB of the satellites in addition to the raw measurements. A variety of PPP positioning models have been developed, among which the un-differenced un-combined scheme shows excellent performance and compatibility. For un-differenced un-combined PPP, the estimated state vector is (using GPS+BDS PPP as an example):

$$\mathbf{x} = [\mathbf{X}_r, dt_r^G, \mathbf{isb}^C, ZWD_r, \mathbf{I}_{r,1}^G, \mathbf{N}_{r,1}^G, \mathbf{N}_{r,2}^G, \mathbf{N}_{r,1}^C, \mathbf{N}_{r,2}^C] \quad (3)$$

Table 1. Dynamic models of navigation states

State	Dynamic characteristic
Position of receiver	Constant (Static); Constant velocity or acceleration (Dynamic)
Receiver clock error	First-order Markov or random walk
Inter-system deviation	First-order Markov or random walk
Tropospheric wet delay	First-order Markov or random walk
Ionospheric delay	First-order Markov or random walk
Integer cycle ambiguity	Constant; Reset covariance when a cycle slip detected

The measurement vector and the measurement matrix are given as follows:

$$\begin{aligned}
 \mathbf{z} &= \begin{bmatrix} p_{r,1}^{1,G} \\ p_{r,2}^{1,G} \\ l_{r,1}^{1,G} \\ l_{r,2}^{1,G} \\ \vdots \\ p_{r,1}^{m,C} \\ p_{r,2}^{m,C} \\ l_{r,1}^{m,C} \\ l_{r,2}^{m,C} \end{bmatrix}, \\
 \mathbf{H} &= \begin{bmatrix} \mathbf{e}_r^{1,G} & 1 & 0 & M_{w_r}^{1,G} & 1 & \cdots & 0 & 0 & \cdots & 0 & \cdots & 0 & \cdots & 0 \\ \mathbf{e}_r^{1,G} & 1 & 0 & M_{w_r}^{1,G} & \gamma_2^G & \cdots & 0 & 0 & \cdots & 0 & \cdots & 0 & \cdots & 0 \\ \mathbf{e}_r^{1,G} & 1 & 0 & M_{w_r}^{1,G} & -1 & \cdots & 0 & 1 & \cdots & 0 & \cdots & 0 & \cdots & 0 \\ \mathbf{e}_r^{1,G} & 1 & 0 & M_{w_r}^{1,G} & -\gamma_2^G & \cdots & 0 & 0 & \cdots & 1 & \cdots & 0 & \cdots & 0 \\ \vdots & \vdots & \vdots & \vdots & \vdots & \ddots & \vdots & \vdots & \ddots & \vdots & \vdots & \vdots & \ddots & \vdots \\ \mathbf{e}_r^{m,C} & 1 & 1 & M_{w_r}^{m,C} & 0 & \cdots & 1 & 0 & \cdots & 0 & 0 & 0 & \cdots & 0 \\ \mathbf{e}_r^{m,C} & 1 & 1 & M_{w_r}^{m,C} & 0 & \cdots & \gamma_2^C & 0 & \cdots & 0 & 0 & 0 & \cdots & 0 \\ \mathbf{e}_r^{m,C} & 1 & 1 & M_{w_r}^{m,C} & 0 & \cdots & -1 & 0 & \cdots & 0 & 0 & 1 & \cdots & 0 \\ \mathbf{e}_r^{m,C} & 1 & 1 & M_{w_r}^{m,C} & 0 & \cdots & -\gamma_2^C & 0 & \cdots & 0 & 0 & 0 & \cdots & 1 \end{bmatrix}
 \end{aligned} \tag{4}$$

where $\mathbf{e}_r^{s,T}$ is the line of sight vector. Based on Table 1 and Eq. (4), the state vector can be estimated using a KF, and this forms the fundamental of PPP.

The major shortcoming of PPP is the long convergence time. PPP-RTK solves this problem by using regional atmospheric corrections and the real-time satellite UPD. Note that ambiguity resolution is not considered here, and thus UPDs are not used.

The measurement vector and Jacobi matrix corresponding to the atmosphere augmentation product are shown in Eq. (5):

$$\mathbf{z} = \begin{bmatrix} zwd_r \\ ion_{r,1}^{1,G} \\ \vdots \\ ion_{r,1}^{m,C} \end{bmatrix}, \mathbf{H} = \begin{bmatrix} 0_{1 \times 3} & 0 & 0 & 1 & 0 & \cdots & 0 & 0 & \cdots & 0 \\ 0_{1 \times 3} & 0 & 0 & 0 & 1 & \cdots & 0 & 0 & \cdots & 0 \\ \vdots & \vdots & \vdots & \vdots & \vdots & \cdots & 0 & 0 & \cdots & 0 \\ 0_{1 \times 3} & 0 & 0 & 0 & 0 & \cdots & 1 & 0 & \cdots & 0 \end{bmatrix} \quad (5)$$

in which zwd and ion are respectively the troposphere and ionosphere measurements. Note that the ionosphere corrections are given in a between-satellite single-differenced way, with the following single-difference matrix:

$$\mathbf{A}_{sd} = \begin{bmatrix} 1 & 0 & 0 & -1 & 0 & 0 \\ 0 & 1 & 0 & -1 & 0 & 0 \\ \vdots & \vdots & \ddots & \vdots & \ddots & \vdots \\ 0 & 0 & 0 & -1 & 0 & 1 \end{bmatrix} \quad (6)$$

When determining the matrix above, we need to select a reference satellite. And in the single-difference matrix, all the elements in the corresponding columns of the reference satellite are -1 . After applying the single-difference operation, the actual measurement vector and the measurement matrix are given by:

$$\mathbf{z}_{sd} = \mathbf{A}_{sd}\mathbf{z}, \mathbf{H}_{sd} = \mathbf{A}_{sd}\mathbf{H} \quad (7)$$

On the basis of (4), PPP-RTK further extends the atmosphere corrections in (7) in the filter. Since ambiguity resolution is not considered in this paper, the PPP-RTK algorithm is actually a kind of atmosphere-augmented PPP. In future work, we will further consider the ambiguity resolution process.

Finally, it is noteworthy that PPP and PPP-RTK filters also depend on error covariance information, including the process noise covariance and the measurement noise covariance, which will be given in Sect. 3.

3 User-End Integrity Monitoring of PPP-RTK

3.1 PPP-RTK Integrity Monitoring Framework

Figure 1 shows the framework of PPP-RTK integrity monitoring, which consists of the server-side integrity monitoring, the performance evaluation of the service products, and the other is the user-end integrity monitoring algorithm. The server-side real-time integrity monitoring aims to reduce the fault probability of service products, and the performance evaluation of service products provides the necessary input information for user-side integrity monitoring, i.e., Integrity Support Message (ISM).

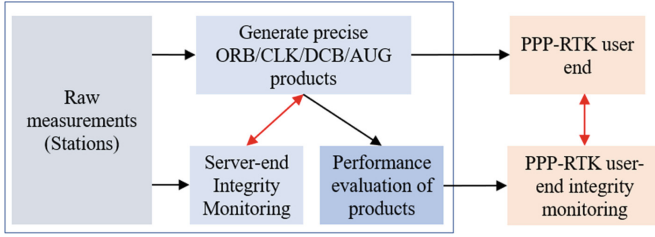


Fig. 1. Top-level integrity monitoring architecture for PPP-RTK

ISM includes the fault probabilities of: (a) the precise orbit and clock, p_{SIS}^s ; (b) the DCB products, p_{DCB}^s ; (c) the troposphere products, p_{TRP}^s ; (d) the ionosphere products, p_{ION}^s ; (e) the event that all ionosphere products are faulted, $p_{\text{ION}}^{\text{all}}$; (f) the measurement faults due to undetected cycle slips and NLOS, p_{USR}^s . Therefore, the fault probability of a single satellite (not the reference satellite) is calculated as follows:

$$p^s = p_{\text{SIS}}^s + p_{\text{DCB}}^s + p_{\text{ION}}^s + p_{\text{USR}}^s \quad (8)$$

The overall fault probability of ionospheric products is calculated as follows:

$$p^{\text{ion}} = p_{\text{ION}}^{\text{all}} + p_{\text{ION}}^{\text{ref}} \quad (9)$$

where $p_{\text{ION}}^{\text{ref}}$ is the fault probability of the ionosphere correction product of the reference satellite.

The error information is also contained in ISM, including: process noise standard deviations of (a) inter-system bias, (b) troposphere delay, and (c) ionosphere delay; measurement noise standard deviations of (a) pseudorange/carrier measurements for each signal of each satellite, (b) troposphere delay products, and (c) ionosphere delay products. Note that we do not make any assumption about the dynamic models of the user position and the receiver clock. And it is noteworthy that the white noise components of the signal-in-space ranging error and the DCB errors are accounted in the pseudorange measurement noise standard deviation. Based on ISM, the measurement noise covariance matrices can be obtained based on (4), (5) and (7), and the conservative state error covariance matrix \mathbf{P} can be calculated in the filtering process.

3.2 MHSS-Based PPP-RTK User-End Fault Detection Algorithm

Real-time fault detection is important for user-side integrity monitoring. In this paper, fault detection is realized based on MHSS. First, the fault modes that need to be monitored are determined. For PPP-RTK users, there are many possible fault modes, but the probability of most modes is very low. Therefore, monitoring only a small part of them is enough. In this work, the determination of monitored fault modes follows the baseline method given in [3].

Table 2. Relationship between fault modes and subfilters

Fault modes	Filter features
Fault-free	Fuse the measurements of all satellites and atmospheric correction measurements
Single satellite fault	Remove all the measurements of the faulted satellite
Troposphere product fault	Remove tropospheric correction measurements
Fault of all ionosphere products	Remove the ionospheric correction measurements
Multiple faults	Remove all the faulted measurements

MHSS-based integrity monitoring scheme requires to run multiple filters in parallel. Each monitored fault mode corresponds to a filter, in which the fault-free mode corresponds to the main filter and the others correspond to the subfilters. The relationship between various fault modes and filters is shown in Table 2.

Fault detection is based on the estimated state vector ${}^i\hat{\mathbf{x}}$ and the state error covariance ${}^i\hat{\mathbf{P}}$ of each filter, where the left superscript i represents the index of monitored fault mode ($i = 0, 1, 2, \dots, N_F$) and $i = 0$ represents the fault-free mode. The states and covariance only consider the position vector, which are expressed in the local East-North-Up (ENU) frame. For each mode $i \neq 0$, the following test is performed [3]:

$$\left| {}^i_q\hat{\mathbf{x}} - {}^0_q\hat{\mathbf{x}} \right| \leq K_{fa,q} {}^i\sigma_{ss,q} \quad (10)$$

where $q = 1, 2, 3$ denote the east, north and up direction in turn; $\sigma_{ss,q}$ is the standard deviation of solution separation in the q th direction; $K_{fa,q}$ is a coefficient determined by the false alarm rate. The calculation methods of $\sigma_{ss,q}$ and $K_{fa,q}$ are shown in (11) and (12), respectively:

$${}^i\sigma_{ss,q} = \sqrt{\mathbf{e}_q^T ({}^i\mathbf{P} - {}^0\mathbf{P}) \mathbf{e}_q} \quad (11)$$

$$K_{fa,q} = Q\left(\frac{p_{fa,q}}{2N_F}\right) \quad (12)$$

where \mathbf{e}_q is a 3×1 vector with its q th element is 1 and the others are 0; $Q(p)$ is the $(1 - p)$ quantile of a unit-variance zero-mean normal distribution; $p_{fa,q}$ is the false alarm rate allocated to the q th direction.

The navigation system is declared as fault-free only if all the tests in (10) pass; otherwise, the system will issue an alarm to remind the user that there is a fault in the system. The protection levels can only be calculated when there is no fault alarm.

3.3 Protection Level Calculation

Protection level is the error upper bound under a given integrity risk (i.e., p_{HMI}). The protection level is defined as:

$$p_{\text{HMI},q} = P\left(\left|{}^0_q\hat{\mathbf{x}} - {}_q\mathbf{x}\right| < PL_q, \text{no fault alert}\right) \quad (13)$$

in which ${}_q\mathbf{x}$ is the true value of state, P is the probability of the event inside the brackets. MHSS provides a direct method to calculate the protection levels [3] as:

$$p_{\text{HMI},q} - \frac{p_{\text{HMI},q}}{p_{\text{HMI}}} p_{\text{NM}} = 2Q\left(\frac{PL_q}{{}_q^0\sigma}\right) + \sum_{i=1}^{N_F} Q\left(\frac{PL_q - K_{fa,q}^i \sigma_{ss,q}^i}{{}_q^i\sigma}\right) \cdot P({}^iH) \quad (14)$$

where p_{NM} is the probability of unmonitored fault modes, ${}_q^i\sigma$ is the state error standard deviation of the q th position state associated with the i th filter, and iH represents the i th fault mode.

4 Experiments and Results

Experiments are carried out to evaluate the performance of the user-end integrity monitoring algorithm of PPP-RTK. The GNSS raw measurements were collected in a static station in Jiangsu Province, and PPP-RTK service products are provided by GeSpace. The test data come from the static station is used to simulate a dynamic scenario by considering the receiver positions at two epochs to be totally independent.

Figure 2 shows the position errors of atmosphere-augmented PPP (namely PPP-RTK in this work, although this may be not rigorous). As shown in this figure, the horizontal position error and the vertical position error quickly converge to less than 1 decimetre and 2 decimetres, respectively. Then, Fig. 3 shows the theoretical accuracy of PPP-RTK, which is clearly in line with the results shown in Fig. 2.

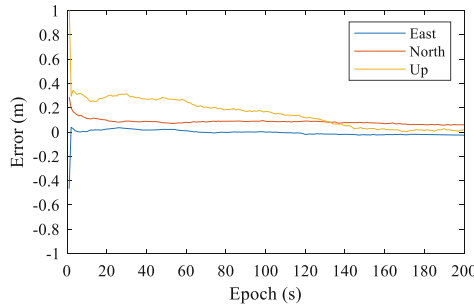


Fig. 2. Position error of PPP-RTK with float ambiguity

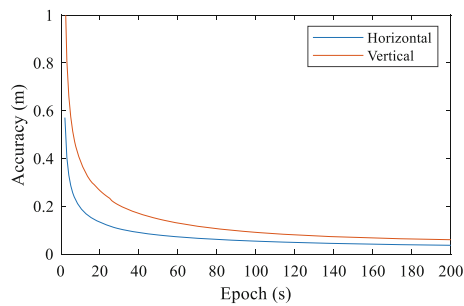


Fig. 3. Theoretical accuracy of PPP-RTK with float ambiguity

Then, the PLs of PPP-RTK are evaluated in four cases and the results are shown in Figs. 4 and 5. The results show that the PLs are obviously different in four cases, and more specifically, the PLs are lower when the fault probability is low. Besides, the results also indicate that under the experiment condition, PPP-RTK can provide the position solution with submeter-level protection levels (99.99999% confidence).

Table 3. Input parameters to integrity monitoring algorithm

Navigation requirement	p_{HMI} , p_{fa} , etc.	Consistent with [3]
Error parameters	Pseudorange/carrier error variance, process noise variance of tropospheric delay and ionospheric delay	Consistent with [11]
	Standard deviation of troposphere product error	0.1 m
	Standard deviation of ionosphere product error	0.2 m
Fault probability	Case1	0
	Case2	Satellite: 10^{-5} ; others: 0
	Case3	Satellite/troposphere: 10^{-5} ; others: 0
	Case4	Satellite/troposphere/ionosphere: 10^{-5}

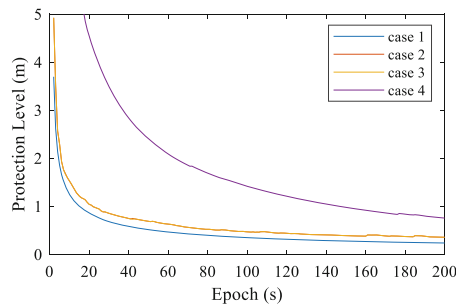


Fig. 4. HPL of PPP-RTK with float ambiguity

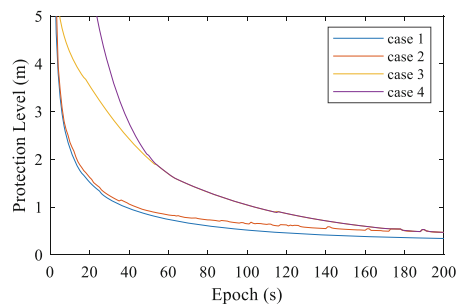


Fig. 5. VPL of PPP-RTK with float ambiguity

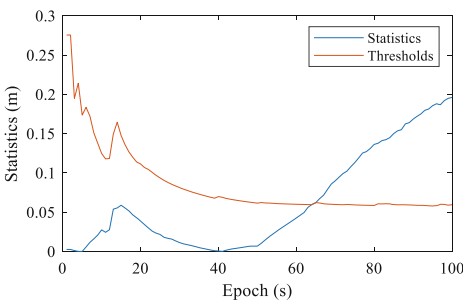


Fig. 6. Fault detection results (fault occurs in 50–100 s)

Finally, the fault detection capability is validated using fault simulation. A 5-m satellite clock fault is simulated and injected to G30 from 50 to 100 s. Figure 6 shows the test statistics and the threshold for one of the solution separation tests. Figure 6 suggests that the fault detector can timely detect the measurement faults. More fault scenarios will be simulated to test the algorithm in the future work.

5 Conclusions

A user-end integrity monitoring algorithm for PPP-RTK is proposed based on multiple hypothesis solution separation. This algorithm includes real-time fault detection and protection level calculation. It considers not only the measurement faults due to heavy multipath and undetected cycle slip but also the faults coming from the service products. Experiments are carried out, and the results suggest the effectiveness of the proposed algorithm. The results also show that the protection levels of the float position solution of PPP-RTK are at a submeter level (the integrity risk is $10^{-7}/h$). Our future work will focus on designing (a) integrity monitoring algorithm of PPP-RTK considering incorrect ambiguity resolution and (b) efficient fault exclusion algorithm.

References

1. Zhu, N., Marais, J., Betaille, D., et al.: GNSS position integrity in urban environments: a review of literature. *IEEE Trans. Intell. Transp. Syst.* **19**(9), 2762–2778 (2018)
2. Brown, R.G.: A baseline GPS RAIM scheme and a note on the equivalence of three RAIM methods. *Navigation* **39**(3), 301–316 (1992)
3. Blanch, J., et al.: Baseline advanced RAIM user algorithm and possible improvements. *IEEE Trans. Aerosp. Electron. Syst.* **51**(1), 713–732 (2015)
4. Odolinski, R., Teunissen, P.J.G.: Low-cost, high-precision, single-frequency GPS–BDS RTK positioning. *GPS Solut.* **21**(3), 1315–1330 (2017)
5. Zhao, Q., Guo, J., et al.: A variant of raw observation approach for BDS/GNSS precise point positioning with fast integer ambiguity resolution. *Satellite Navigat.* **2**(1), 20 (2021)
6. Teunissen, P.J.G., Khodabandeh, A.: Review and principles of PPP-RTK methods. *J. Geodesy* **89**(3), 217–240 (2015)
7. Tanil, C., Khanafseh, S., Joerger, M., et al.: Optimal INS/GNSS coupling for autonomous car positioning integrity. In: *Proceedings of the 32nd International Technical Meeting of the Satellite Division of the Institute of Navigation (ION GNSS+ 2019)*, pp. 3123–3140 (2019)
8. Wang, S., Zhan, X., Zhai, Y., et al.: Ensuring high navigation integrity for urban air mobility using tightly coupled GNSS/INS system. *J. Aeronaut. Astronaut. Aviat.* **52**(4), 429–442 (2020)
9. Gunning, K., Blanch, J., Walter, T., et al.: Design and evaluation of integrity algorithms for PPP in kinematic applications. In: *Proceedings of the 31st International Technical Meeting of the Satellite Division of the Institute of Navigation (ION GNSS+ 2018)*, pp. 1910–1939 (2018)
10. Rodriguez-Solano, C., et al.: Protection level of the trimble RTX positioning engine for autonomous applications. In: *Proceedings of the 34th International Technical Meeting of the Satellite Division of the Institute of Navigation (ION GNSS+ 2021)*, pp. 1577–1595 (2018)
11. Zhou, F.: Theory and methodology of multi-GNSS undifferenced and uncombined precise point positioning. Ph.D. Thesis, East China Normal University (2018)